Infrared limb sounding of Titan with the Cassini Composite InfraRed Spectrometer: effects of the mid-IR detector spatial responses

Conor A. Nixon,[1,2,*] Nicholas A. Teanby,[3] Simon B. Calcutt,[3] Shahid Aslam,[2,4]
Donald E. Jennings,[2] Virgil G. Kunde,[1,2] F. Michael Flasar,[2] Patrick G. J. Irwin,[3]
Fredric W. Taylor,[3] David A. Glenar,[2] and Michael D. Smith[2]

[1]University of Maryland, Department of Astronomy, College Park, Maryland 20742, USA

[2]NASA Goddard Space Flight Center, Planetary Systems Branch, Greenbelt, Maryland 20771, USA

[3]University of Oxford, Sub-Department of Atmospheric, Oceanic, and Planetary Physics,
Clarendon Laboratory, Parks Road, Oxford OX1 3PU, UK

[4]MEI Technologies Inc., 2525 Bay Area Boulevard, Suite 300, Houston, Texas 77058, USA

*Corresponding author: conor.a.nixon@nasa.gov

The composite infrared spectrometer (CIRS) instrument on board the Cassini Saturn orbiter employs two 1×10 HgCdTe detector arrays for mid-infrared remote sensing of Titan's and Saturn's atmospheres. In this paper we show that the real detector spatial response functions, as measured in ground testing before launch, differ significantly from idealized "boxcar" responses. We further show that neglecting this true spatial response function when modeling CIRS spectra can have a significant effect on interpretation of the data, especially in limb-sounding mode, which is frequently used for Titan science. This result has implications not just for CIRS data analysis but for other similar instrumental applications. © 2009 Optical Society of America

OCIS codes: 010.0280, 010.1280, 040.3060, 040.5160, 120.0280, 300.6340.

1. Introduction

Launched on 15 October 1997, the Cassini spacecraft is NASA's flagship mission to the Saturn system and carries onboard a varied payload of 12 scientific instruments. Mid- and far-infrared spectroscopy is performed by the Composite InfraRed Spectrometer (CIRS) [1,2], the conceptual successor to the Infra-Red Interferometer Spectrometer (IRIS) [3] that flew on Voyagers 1 and 2. Since achieving Saturn orbit on 1 July 2004, Cassini has now completed over 70 orbits of Saturn and more than 45 targeted flybys of Titan, along with many more of the smaller satellites. Close encounters with Titan, and also periapse

encounters with Saturn, allow CIRS to perform its most challenging but extremely important limb-sounding measurements, where the detectors are placed above the horizon at successive altitudes to allow the retrieval of vertical temperature and composition profiles. These are most useful when the projected size of an infrared detector resolves an atmospheric scale height or less of the body—the altitude increment in which the pressure drops by $1/e$—about 50 km for the stratospheres of both Titan and Saturn.

The successful inversion of CIRS spectra requires accurate modeling of the emerging radiation field. For surface-intercepting (on-disk) spectra, especially for small fields and low emission angles, the homogeneity of the field of view usually permits simple modeling with a single ray calculated for the detector

center. For limb spectra, however, due to the rapid decrease in atmospheric density with altitude, and concomitant gradients in the temperature and gas volume mixing ratio (VMR) profiles, the uniform field approximation is expected to be less suitable, and the data will generally require modeling by consideration of multiple rays. However, an exception may be made for small fields with short integration times (low signal-to-noise, S/N), where systematic errors introduced by uniform-field modeling are outweighed by spectral noise.

Most early analyses of CIRS Titan limb spectral averages have, in fact, used this "infinitesimal field" approximation. In some studies [4–7], the number of spectra in each bin was fairly small (typically ∼30) and, therefore, the lack of spatial convolution was presumed inconsequential compared to random and systematic errors in the dataset. Later studies, however, [8,9] have sought to analyze larger limb averages (∼100–200 spectra) and, while successfully modeling most gas emission to reveal the signatures of new isotopic species, some residual model error reported may be attributable to the use of the infinitesimal approximation.

In a recent paper [10] Teanby and Irwin sought to quantify the effect of the finite field of view (FOV) of CIRS on limb sounding of Titan. By modeling the three different detector types (see Subsection 2.A) with idealized spatial two-dimensional (2D) response functions (Gaussian, boxcar), they demonstrated that the finite FOV width can indeed have a significant effect on measured radiances. This has prompted a switch to modeling with a finite FOV convolution in more recent analyses of CIRS Titan limb data [11–14].

In reality, the spatial responses of the CIRS detectors differ substantially from simple analytical functions; moreover, the response is not in general symmetric about the detector center. Fortunately, detailed measurements of the mid-infrared spatial response were made during prelaunch assembly and test [15]. This information has prompted us to examine the question of whether these actual detector spatial responses have a measurable effect on mid-infrared limb sounding of Titan in realistic scenarios or not, and whether previously published results are valid in the light of these findings. In this paper, we first describe the experimental measurements and results, and then apply the real spatial response functions to radiative transfer calculations and retrievals for simulated and actual Titan data.

2. Laboratory Measurements

A. Instrument Overview

CIRS consists of two spectrometers that share common primary (508 mm) and secondary (76 mm) mirrors, fore-optics, reference laser, and even scan mechanism—as shown in the optical schematic (Fig. 1). The field is divided at a mirror into the far-infrared (FIR) polarizing interferometer
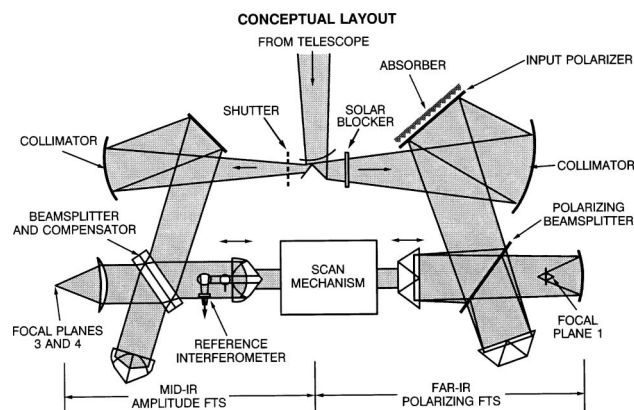

Fig. 1. Schematic diagram of CIRS optical layout. CIRS consists of two interferometers (left side = MIR, right side = FIR) sharing a common telescope, scan mechanism, and reference laser. See text for details.

(Martin–Puplett type, [16]) and the mid-infrared (MIR) Michelson interferometer. The FIR interferometer signal is detected by a single bolometer detector (Focal Plane 1, hereafter FP1), which has an approximately Gaussian spatial response of FWHM 2.5 mrad, and sensitivity from 10–600 cm^{-1} (1 mm–17 μm). [Focal plane 2 (FP2) from the initial design was eliminated in a descope.]

The MIR interferometer recombined beam reaches the MIR focal plane assembly (FPA), consisting of two 1×10 HgCdTe detector arrays, FP3 and FP4. FP3 is of photoconductive type (PC), sensitive to 600–1100 cm^{-1} (17–9 μm), while FP4 is of photovoltaic (PV) design and covers the spectral range 1100–1500 cm^{-1} (9–7 μm). The scan mirror maximum travel is up to 2 cm, which allows a variable spectral resolution between 15.5–0.5 cm^{-1}, where the lowest resolution (shortest scan) is constrained by the short, invariable travel at negative path difference (before zero path-difference (ZPD) fringe) needed to provide the low-resolution two-sided interferogram. Further details of the instrument have been previously published [1,2].

The PC and PV detectors are of fundamentally different design and operating principles, as described in standard texts (e.g., [17]). We concern ourselves here with the CIRS implementation, which has important considerations for the detector spatial responses. A schematic of the MIR layout is shown in Fig. 2. Both 1×10 arrays have detector sizes of 200 μm and pitches (center-to-center spacing) of ∼215 μm.

The PV detectors of FP4 are photodiodes, each comprised of two different layers of HgCdTe semiconductor—p doped and n doped—joined together to create a junction layer. Photons reaching this layer create electron-hole pairs, the electrons being attracted to the p side and the holes being attracted to the n side, and thus a measurable voltage. A key physical characteristic is that the detector spatial response, like the junction layer, is square and nearly uniform.
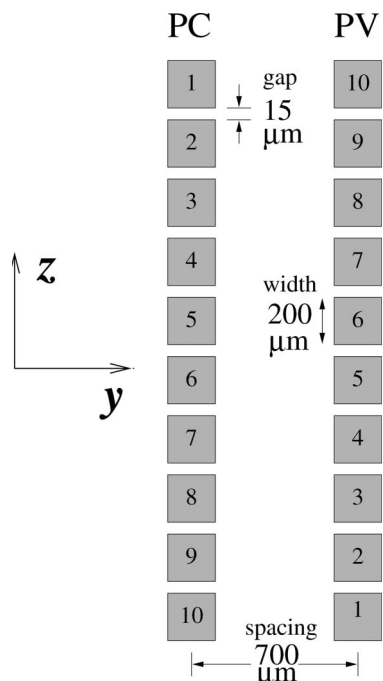
Fig. 2. CIRS MIR focal plane layout.

The PC detectors measure the change in conductivity when a photon strikes the material, promoting an extra electron to the conduction band, which is of similar width to the energy of an infrared photon. The CIRS PC detectors are formed in a U-shape (Fig. 3), allowing the positive and negative contacts to be placed on the same side and, therefore, in closer proximity to the PV array (FP4) on the opposite side. Note the implication of this layout: that the detector "beam" or spatial response will follow the semiconductor, and also be U-shaped.

Each detector array was physically mounted on metal subcarriers during original manufacture: titanium for FP3 and copper for FP4. These were subsequently mounted onto the MIR FPA, consisting of a tripod, imaging lens, and reference plate, for alignment and response testing. Later, these optical elements were connected to the thermal control elements: cold finger, attached to a passive radiative cooler, and replacement heater. The nominal operating temperature range is 75–85 K.

B. Mid-Infrared Field-of-View Measurements

During the period of November 1995 to May 1996, the MIR FPA was assembled and tested in the Space Instruments Laboratory at Oxford University, prior to integration of the entire instrument at NASA Goddard Space Flight Center (GSFC). A key component of the MIR optical subsystem testing at Oxford was to ensure the correct distances and alignment of the detectors and lens assembly. The alignment testing also provided the opportunity to image the MIR focal plane and to measure the spatial response characteristics of all MIR detectors, measurements that we show in Section 3 to be of importance for modeling and interpreting spectra.
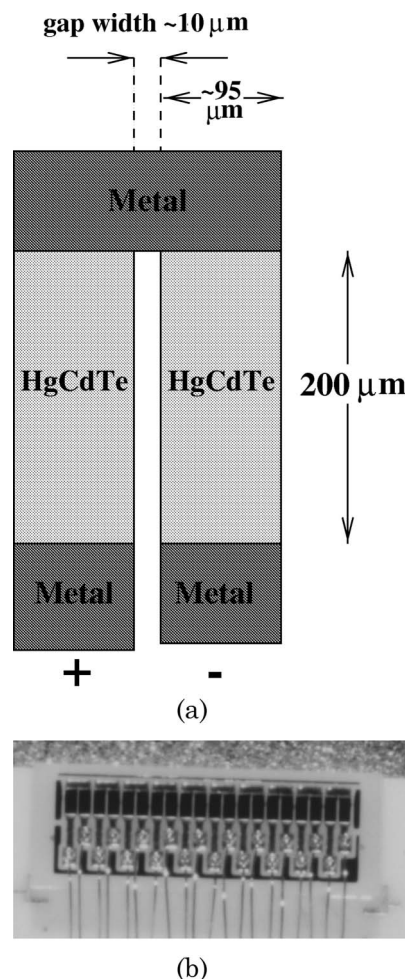

(a)

(b)

Fig. 3. (a) CIRS photoconductive (PC) detector schematic. Ten PC detectors in a linear array are known as CIRS focal plane 3 (FP3) and cover the spectral range of 600–1100 cm^{-1}. (b) Photograph of the flight PC array taken at NASA GSFC. The detectors appear as pairs of dark rectangles above the gold contacts.

The alignment testing was performed in an evacuated vacuum tank, with the FPA cooled to operating temperature ($\sim$77 K) by liquid nitrogen, taking the role performed by the passive radiative cooler in space. The alignment test rig (ATR) is depicted in Fig. 4. Radiation from a globar (1000 K) was chopped before passing through a pinhole (20 μm diameter, chosen to avoid diffraction at the longest wavelengths), providing a "point" source. The FPA is designed to receive collimated radiation from the interferometer in normal operation; therefore, in the ATR a second, identical lens was used in reverse configuration to provide a collimated beam to the imaging lens. The dual 55.4 mm lenses were fabricated from diamond-turned germanium, with coatings of PbTe, ZnSe, and BaF$_2$, an f-number of 1.45 and a 70% diffraction-limited spot size of 12.4 μm. The pinhole was provided with a positioning system accurate to $\pm 1 \mu$m, enabling movement in three orthogonal directions. The coordinate system was established by a reference plate to which the FPA was attached; all other coordinates (e.g., collimating lens reference
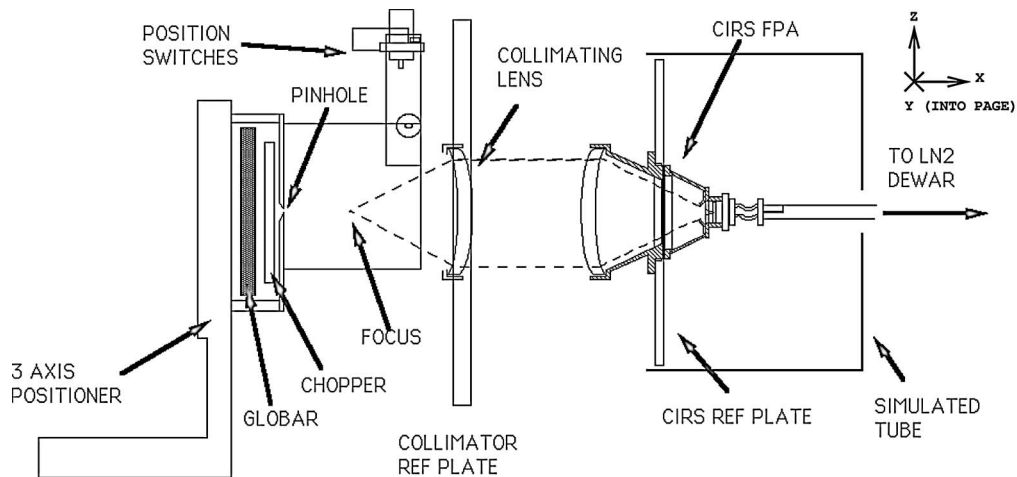
Fig. 4. Diagram of the CIRS alignment test rig, which was used to test the focusing and alignment of the MIR focal plane assembly (FPA = FP3 and FP4 arrays). The entire apparatus was sealed inside an evacuated vacuum chamber during the testing.

plate) could therefore be transformed into this frame (FPA coordinates).

Details of focusing and alignment are given in [15] and are briefly summarized here. This was accomplished by scanning the pinhole in the image plane of the detectors, and measuring their response signals to locate the detectors exactly in all three dimensions. The arrays were moved in X (perpendicular to the lens) to achieve maximum response (best focus) with an accuracy of $25\,\mu m$, and the detector carriers were also shimmed to achieve alignment in the Y and Z directions. After the alignment and focusing was complete, the pinhole was scanned through the image plane in the Y and Z directions at a step size of $20\,\mu m$ and the detector signals recorded, thereby enabling the 2D spatial response of all 20 detectors to be recorded in their final configuration.

C. Results of Subsystem Testing

Figure 5 shows the responses of all 20 detectors, measured on 10 April 1996 (18 months before Cassini launch), plotted as amplitude contours. We can see immediately the difference between the relatively flat, uniform plateau of response for the PV detectors (FP4), compared to the bifurcated response of the PC detectors (FP3), as expected from manufacture. In addition, there is a greater detector-to-detector variation both in amplitude and shape for the PCs, compared to the PVs. Figure 6 shows the response for the four end-of-array detectors plotted as three-dimensional (3D) wire-frame diagrams, based on $10\,\mu m$ resolution scans that were made of these detectors only. Again the differences are striking: between the regular, boxcarlike PVs and the bifurcated PCs, and also between PC01 and PC10. PC01 has a much more asymmetric response in the two lobes than any of the other detectors.

The long axis of the two response lobes for the PC detectors (Y direction) is perpendicular to the array direction (Z), which is often placed perpendicular to the disk edge of Titan or Saturn during limb sounding to obtain a vertical profile of temperature and gas abundance. Emitted radiances can vary rapidly with altitude, whereas horizontal variations over similar distances can be neglected, and so Z variations (cross lobe) in response are generally more important in the
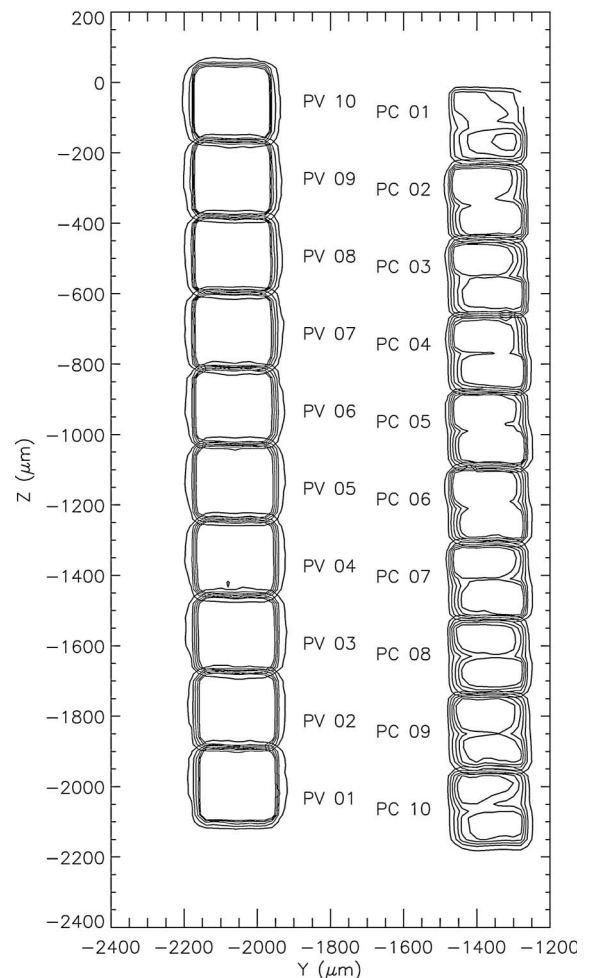

Fig. 5. Contour plot of FP3 and FP4 detector responses, from $20\,\mu m$ resolution scans. Y and Z are in micrometers, and the contour levels are 100, 200, 300, 400, and 500 raw counts.
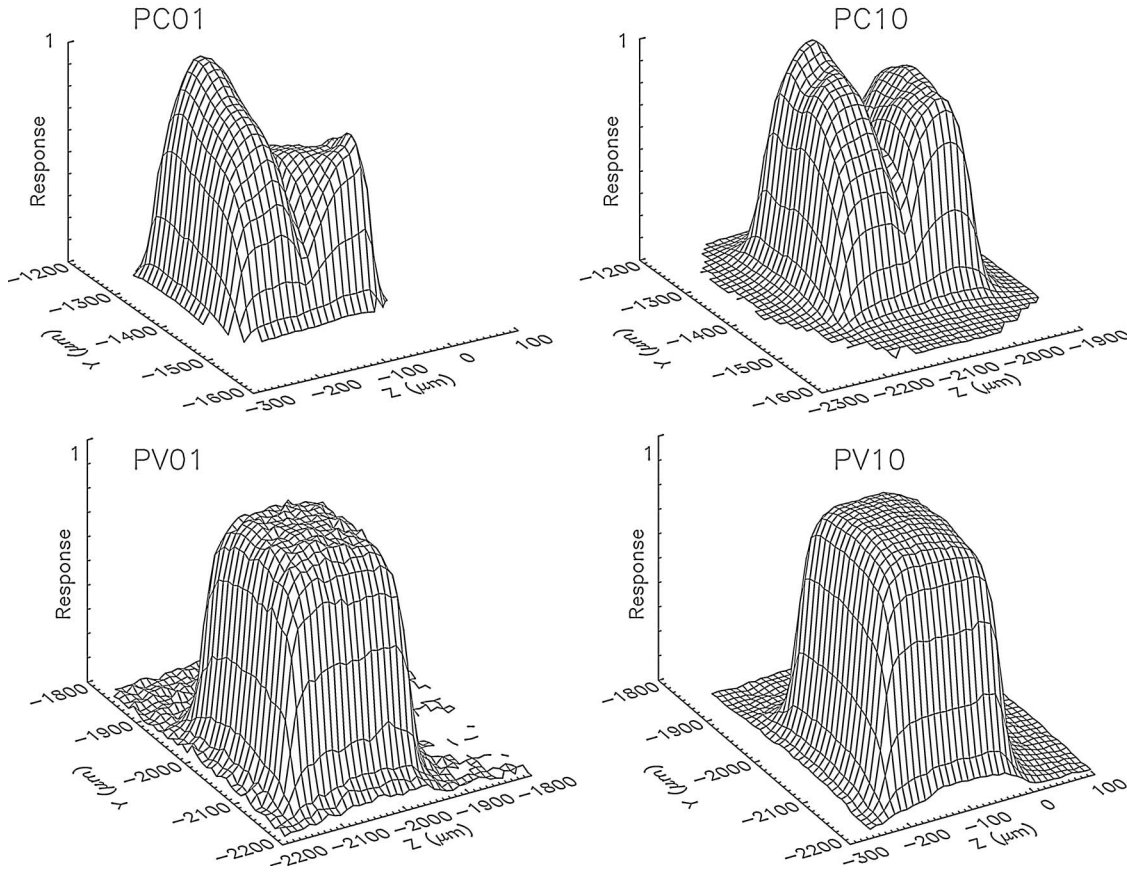
Fig. 6. 3D view of responses for four array-end detectors of FP3 and FP4, from 10 μm resolution scans. Y and Z are in micrometers, while the response is in arbitrary counts. The PV detectors have a nearly table-top response plateau, while the PC detectors show a bifurcated dual-lobe response. In addition, PC01 is much less symmetric than PC10; see also Fig. 7.

measurement process than Y variations (along each lobe). We therefore collapse the 2D detector responses onto Y-averaged Z cross sections as follows.

Let $R_n(Y_j, Z_k)$ be the measured response function of detector n, at the grid position specified by (Y_j, Z_k). The absolute maximum of each detector is given by $R_{\mathrm{MAX}}(n)$. We first define a 2D masking function $W_n(Y_j, Z_k)$ as follows:

$$W_n(Y_j, Z_k) = \begin{cases} 1 & R_n(Y_j, Z_k) \geq R_{\mathrm{MAX}}(n)/2, \\ 0 & \text{otherwise} \end{cases} \quad (1)$$

which defines the interior of each detector, within limits given by the half-maximum response, and may form an irregular perimeter. The geometric centroid $(\bar{Y}_n, \bar{Z}_n)$ of the nth detector (not response weighted) is then given by the mean Y and Z values within the half-power perimeter (to ignore irregular low-amplitude edges):

$$\bar{Y}_n = \frac{\sum_j [Y_j \sum_k W_n(Y_j, Z_k)]}{\sum_{j,k} W_n(Y_j, Z_k)}, \quad (2)$$

$$\bar{Z}_n = \frac{\sum_k [Z_k \sum_j W_n(Y_j, Z_k)]}{\sum_{j,k} W_n(Y_j, Z_k)}. \quad (3)$$

Table 1 gives the computed centroids and FWHMs (both directions) for all 20 MIR detectors. Several points are of note here. First, the two arrays are somewhat offset in the Z direction from each other in this test data, with FP4 shifted by $\sim +70\,\mu$m (or $\sim 1/4$ pixel) relative to FP3. The veracity of this shift is discussed further in Subsection 2.E. Second, the FWHM responses of the PC detectors (FP3) are smaller in the Y direction than those of the PVs (FP4) by about 8%, although the FWHMs in the Z direction are almost identical.

We now proceed to make Y averages of the detector responses, by taking the mean response within $\pm 100\,\mu$m of $\bar{Y}$:

$$\bar{R}_n(Z_k) = \sum_{Y_j=\bar{Y}_n-100}^{Y_j=\bar{Y}_n+100} R_n(Y_j, Z_k)/\mathrm{MAX}(\bar{R}_n). \quad (4)$$

In Fig. 7 we show a plot of the functions $\bar{R}_n(Z_k)$. These have been normalized to the peak value for each detector, as the mean detector responsivities (counts/irradiance) are determined individually during radiometric calibration and, therefore, only the relative variation within a detector is of importance here. Finally, we spline-interpolated the functions $R_n(Z_k)$ onto a grid of points uniformly spaced from

Table 1. Detector Location and FWHM

Detector	$\bar{Y}(\mu\mathrm{m})$	$\bar{Z}(\mu\mathrm{m})$	$\Delta Y(\mu\mathrm{m})$	$\Delta Z(\mu\mathrm{m})$
PC01	−1371.75	−126.25	181.5	179.0
PC02	−1370.00	−340.00	183.0	190.5
PC03	−1369.53	−558.14	181.5	189.5
PC04	−1368.33	−767.62	181.4	183.5
PC05	−1370.00	−981.86	182.5	189.5
PC06	−1369.21	−1199.89	181.0	190.0
PC07	−1366.97	−1417.87	183.5	191.0
PC08	−1365.06	−1625.40	185.5	190.5
PC09	−1365.17	−1839.21	182.0	191.5
PC10	−1366.09	−2058.48	182.0	192.5
PV01	−2050.91	−1990.91	197.0	191.0
PV02	−2050.11	−1781.10	197.0	191.5
PV03	−2051.84	−1570.00	195.0	193.5
PV04	−2059.05	−1349.33	199.5	195.0
PV05	−2068.16	−1130.00	195.5	193.0
PV06	−2070.00	−917.83	199.5	192.0
PV07	−2069.09	−709.09	198.0	193.0
PV08	−2070.00	−490.00	195.0	193.0
PV09	−2070.00	−270.00	195.0	195.0
PV10	−2070.74	−54.74	198.5	192.0

the centroid of each detector resulting in a regridded one-dimensional (1D) response average $R'_n(Z)$. These values are given in Table 2.

D. Adding the Telescope Point Spread Function

In actuality, this subsystem level measurement of the detector relative spatial responses cannot be directly used to weight the planetary radiation field, as it neglects a further spatial convolution due to the telescope. The telescope has a nonnegligible point spread function (PSF) which, if ignored, will lead to an incorrect spatial response function.

The telescope PSF was also measured during pre-flight testing as an independent subsystem at NASA GFSC, by illuminating the full aperture, contained in a cold dewar, with a plane wavefront from a 632 nm laser source. The encircled energy (EE) distribution was subsequently measured and found to be well modeled by a 2D Gaussian function:

$$G(Y,Z) = \exp\left(-\frac{(y-y_0)^2 + (z-z_0)^2}{\sigma^2}\right), \quad (5)$$

with a best-fit σ of 59 μm [18]. If we ignore off-axis effects, we may convolve all 20 MIR detector spatial responses with this function to emulate the effect of the telescope optics. Finally, we have converted the FPA spatial units (micrometers) to angular units (milliradians) for use in calculations using the conversion: 215 μm = 0.294 mrad on the sky, from the measured detector pitch. The detector response cross sections after convolution are shown in Fig. 8. The centroids and FWHM of the smoothed detector functions are given in Table 3, while the angular response is tabulated in Table 4. The FWHM of the detectors is generally very close to the cannonical value of
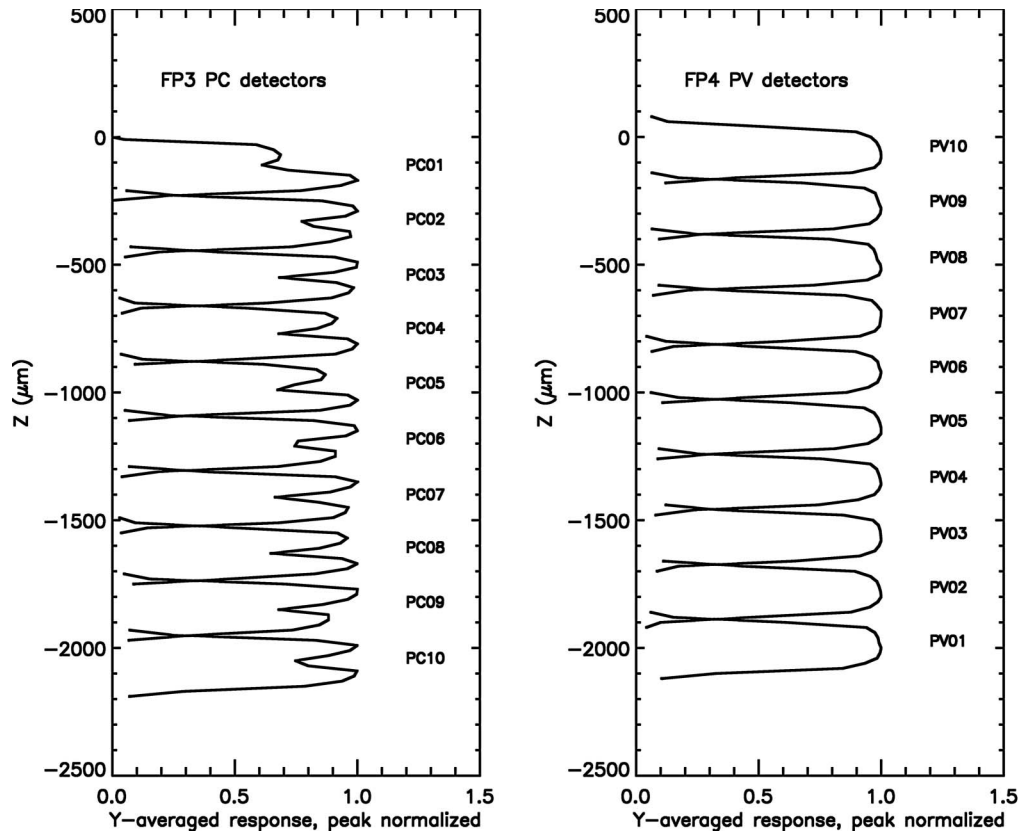

Fig. 7. Responses for all 20 MIR detectors averaged in the Y direction and normalized to the peak value (Z in micrometers). Note the particularly asymmetric response of PC01. See also Table 2 for values.

Table 2. Y-Averaged Detector Responses—Laboratory Scans

$\Delta Z(\mu m)^a$	−140.0	−120.0	−100.0	−80.0	−60.0	−40.0	−20.0	0.0	20.0	40.0	60.0	80.0	100.0	120.0	140.0
PC01	0.042	0.108	0.395	0.843	0.943	1.000	0.933	0.709	0.652	0.713	0.709	0.694	0.554	0.093	0.068
PC02	0.131	0.085	0.479	0.858	0.938	0.995	0.908	0.777	0.863	1.000	0.995	0.973	0.588	0.132	0.082
PC03	0.143	0.048	0.431	0.830	0.948	0.980	0.974	0.752	0.795	0.984	1.000	0.987	0.641	0.211	0.000
PC04	0.000	0.159	0.573	0.931	0.975	1.000	0.925	0.678	0.852	0.895	0.916	0.846	0.502	0.078	0.066
PC05	0.043	0.143	0.540	0.932	0.968	1.000	0.833	0.662	0.792	0.859	0.855	0.778	0.420	0.048	0.120
PC06	0.093	0.086	0.451	0.808	0.887	0.935	0.835	0.727	0.864	0.999	1.000	0.959	0.540	0.101	0.112
PC07	0.124	0.067	0.486	0.863	0.944	0.972	0.920	0.712	0.794	0.965	0.993	1.000	0.604	0.173	0.000
PC08	0.000	0.200	0.576	0.875	0.967	1.000	0.865	0.662	0.883	0.932	0.963	0.850	0.407	0.073	0.088
PC09	0.000	0.203	0.564	0.814	0.849	0.896	0.746	0.741	0.919	0.964	1.000	0.879	0.397	0.052	0.174
PC10	0.069	0.173	0.586	0.898	0.951	1.000	0.879	0.735	0.811	0.929	0.981	0.942	0.498	0.110	0.139
PV01	0.146	0.220	0.603	0.933	0.958	0.996	1.000	0.999	0.992	0.983	0.981	0.841	0.430	0.129	0.193
PV02	0.099	0.138	0.473	0.869	0.956	0.985	1.000	0.998	0.993	0.985	0.959	0.912	0.489	0.172	0.000
PV03	0.199	0.104	0.418	0.823	0.958	0.985	0.997	1.000	0.997	0.995	0.978	0.950	0.615	0.211	0.128
PV04	0.148	0.148	0.532	0.874	0.947	0.987	0.997	1.000	0.994	0.987	0.977	0.899	0.508	0.154	0.168
PV05	0.099	0.213	0.600	0.921	0.967	0.994	1.000	0.997	0.991	0.978	0.969	0.824	0.419	0.121	0.171
PV06	0.000	0.193	0.522	0.891	0.954	0.989	0.997	1.000	0.992	0.985	0.965	0.873	0.458	0.156	0.108
PV07	0.179	0.113	0.412	0.812	0.964	0.985	0.996	0.997	1.000	0.992	0.970	0.946	0.607	0.213	0.085
PV08	0.170	0.131	0.491	0.883	0.977	0.998	1.000	0.991	0.982	0.977	0.963	0.918	0.546	0.147	0.135
PV09	0.135	0.165	0.564	0.924	0.969	0.992	1.000	0.997	0.988	0.981	0.967	0.853	0.439	0.094	0.170
PV10	0.039	0.203	0.547	0.944	0.977	0.998	1.000	0.998	0.991	0.975	0.958	0.835	0.432	0.114	0.136

$^a\Delta Z$ is relative to the Z centroid.

0.273 mrad [1], except for FP3 in the Y direction, where the FWHM is about 7% smaller.

Note that fundamental diffraction limits to optical performance are not reached in the CIRS MIR interferometer. Evaluation of the standard formula for the angular diameter of the first Airy disk, $2a_1 = 2.44\lambda/D$, where λ is wavelength and D is the primary mirror diameter, yields a range of 0.032 mrad (at $\lambda = 7\,\mu m$) to 0.085 mrad (at $\lambda = 17\,\mu m$).

E. Note Regarding Optical Testing of Integrated Instrument

For completeness, it is appropriate here to mention briefly other optical testing of the combined CIRS
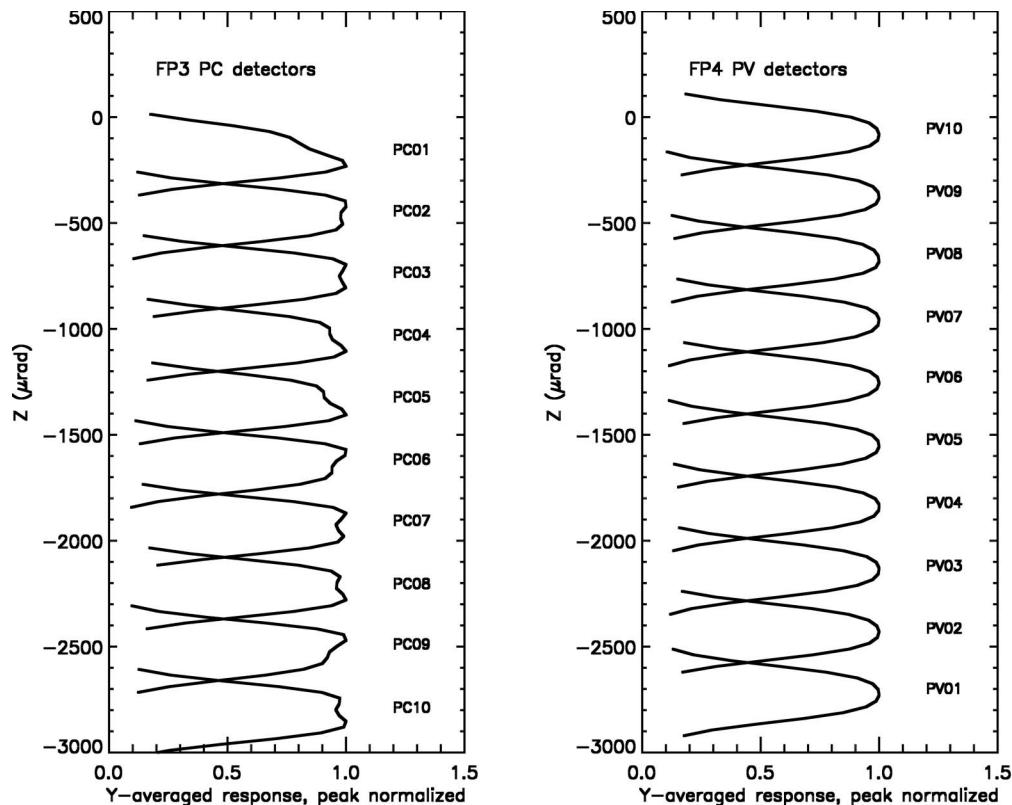

Fig. 8. Responses for all 20 MIR detectors averaged in the Y direction, smoothed with the telescope point spread function as described in the text and normalized to the peak value (Z in milliradians). See also Table 4 for values.

Table 3. Detector Location and FWHM—PSF Smoothed

Detector	$\bar{Y}(\mu\text{rad})$	$\bar{Z}(\mu\text{rad})$	$\Delta Y(\mu\text{rad})$	$\Delta Z(\mu\text{rad})$
PC01	−1869.80	−175.61	252.5	261.1
PC02	−1876.19	−465.55	255.0	274.5
PC03	−1875.18	−756.55	255.9	271.5
PC04	−1868.14	−1052.63	256.4	272.0
PC05	−1870.14	−1345.63	256.0	270.0
PC06	−1871.98	−1640.77	256.5	272.0
PC07	−1869.03	−1930.13	258.2	275.0
PC08	−1868.04	−2229.23	255.9	277.0
PC09	−1869.25	−2514.71	255.5	275.0
PC10	−1868.23	−2814.19	259.0	281.0
PV01	−2806.71	−2725.27	275.0	265.0
PV02	−2807.60	−2432.76	273.3	265.0
PV03	−2808.42	−2144.76	273.0	268.0
PV04	−2816.93	−1846.05	276.0	268.2
PV05	−2820.75	−1547.71	275.0	266.8
PV06	−2826.36	−1257.10	277.2	265.0
PV07	−2828.52	−965.83	275.0	265.0
PV08	−2826.93	−668.72	275.5	268.5
PV09	−2827.93	−371.88	274.0	268.0
PV10	−2831.07	−77.44	273.0	266.5

instrument. These tests fall into two categories: ground testing and in-flight testing. A complete description of these tests is beyond the scope of this paper; however, the analysis is described in a series of internal CIRS team documents, whose overall conclusions are summarized here.

After the subassemblies were finalized, the complete instrument was subjected to both FOV testing and radiometric testing before flight at NASA GSFC [19]. The detector FOV testing was performed using an apparatus similar to that used for the MIR FPA testing, but on a larger scale. The complete instrument was placed in a large thermal vacuum chamber, and a reverse telescope assembly was used to provide a collimated beam from a 1000 K blackbody source located outside the tank. Various pinhole sizes were used, the smallest being 0.058 mrad, or ∼1/5 of a MIR detector. The tests were mainly 1D scans along the arrays (Z direction) and cutting across both arrays (Y direction), although several pixels were subjected to 2D scans (FP3 detectors 1 and 5, and FP4 detectors 6 and 10). The 1D scans of the full arrays show good general agreement with Fig. 8 regarding FWHM (0.286 mrad) and response shape, although the match is not exact as expected, because a 1D section through the detector centers is not an identical function to the 2D scans subsequently collapsed to 1D.

Testing in space was also performed in a similar manner: the planet Jupiter and several bright stars were used as sources, and 1D scan sections were obtained in the Y and Z directions as before. The most extensive test was performed with Jupiter on 28–29 April 2001, when the planet was 1.1×10^8 km distant, yielding a mean angular diameter of 1.24 mrad. This is about four times the size of a CIRS MIR pixel (although half the FWHM for the FP1 bolometer) and so clearly not a point source compared to the MIR detectors. The primary purpose of the testing was to measure the FIR spatial response function, and also to check the centroid (boresight) of the MIR arrays in spacecraft coordinates [20]; individual detector locations and widths were also determined. The results showed a small offset in Z between the two arrays, as seen in the earlier Oxford lab tests, although of lesser amplitude (0.08 pixel). However, the angular size of the target (Jupiter) was probably too great to make a definitive test. Therefore, our conclusion is that the 1/4 pixel shift seen in the laboratory tests is real.

Table 4. Y Averaged Detector Responses—PSF Smoothed

$\Delta\theta(\mu\text{rad})^a$	−210.0-210.0	−180.0	−150.0	−120.0	−90.0	−60.0	−30.0	0.0	30.0	60.0	90.0	120.0	150.0	180.0	210.0
PC01	0.081	0.187	0.389	0.654	0.885	1.000	0.990	0.912	0.840	0.796	0.741	0.616	0.420	0.227	0.065
PC02	0.088	0.204	0.412	0.666	0.871	0.969	0.980	0.971	0.987	1.000	0.938	0.754	0.487	0.248	0.104
PC03	0.074	0.230	0.451	0.711	0.909	0.993	0.990	0.972	0.986	1.000	0.930	0.732	0.462	0.231	0.092
PC04	0.086	0.227	0.451	0.717	0.918	1.000	0.985	0.945	0.934	0.930	0.862	0.687	0.441	0.225	0.079
PC05	0.095	0.226	0.453	0.722	0.927	1.000	0.971	0.921	0.905	0.896	0.821	0.642	0.402	0.200	0.050
PC06	0.080	0.194	0.396	0.639	0.832	0.922	0.935	0.941	0.976	1.000	0.933	0.736	0.464	0.229	0.095
PC07	0.087	0.265	0.501	0.759	0.935	0.992	0.974	0.958	0.983	1.000	0.920	0.709	0.433	0.210	0.084
PC08	0.084	0.218	0.434	0.695	0.905	1.000	0.994	0.965	0.968	0.978	0.914	0.725	0.463	0.237	0.090
PC09	0.110	0.250	0.465	0.692	0.849	0.912	0.924	0.945	0.989	1.000	0.902	0.678	0.403	0.190	0.080
PC10	0.114	0.261	0.494	0.750	0.932	1.000	0.985	0.957	0.963	0.976	0.910	0.717	0.452	0.229	0.101
PV01	0.086	0.205	0.410	0.652	0.845	0.951	0.992	1.000	0.987	0.939	0.819	0.609	0.362	0.167	0.061
PV02	0.071	0.194	0.396	0.639	0.837	0.948	0.991	1.000	0.987	0.938	0.819	0.613	0.370	0.178	0.065
PV03	0.063	0.164	0.354	0.598	0.810	0.935	0.986	1.000	0.993	0.958	0.859	0.670	0.426	0.214	0.086
PV04	0.071	0.183	0.383	0.625	0.824	0.939	0.988	1.000	0.991	0.950	0.841	0.642	0.396	0.191	0.073
PV05	0.087	0.211	0.419	0.660	0.851	0.955	0.994	1.000	0.986	0.935	0.813	0.605	0.362	0.170	0.064
PV06	0.075	0.193	0.388	0.627	0.826	0.941	0.989	1.000	0.990	0.944	0.831	0.631	0.388	0.189	0.066
PV07	0.049	0.177	0.368	0.611	0.817	0.938	0.987	1.000	0.992	0.953	0.848	0.654	0.408	0.199	0.074
PV08	0.079	0.194	0.396	0.643	0.845	0.956	0.996	1.000	0.987	0.945	0.838	0.641	0.394	0.187	0.070
PV09	0.082	0.198	0.401	0.646	0.844	0.952	0.993	1.000	0.987	0.941	0.825	0.621	0.374	0.174	0.065
PV10	0.085	0.205	0.408	0.652	0.850	0.957	0.995	1.000	0.984	0.934	0.815	0.612	0.372	0.181	0.063

[a]$\Delta\theta$ is the same sense as ΔZ.

3. Application of CIRS Spatial Response Functions to Titan

Figure 9 depicts a simplified diagram of the limb-viewing geometry for a single CIRS detector, in vertical section. MIR limb observations are typically performed at 5–9 h (~ 1–2×10^5 km) from Titan's closest approach, when the 0.27 mrad detectors subtend ~ 30–60 km on the limb, or about one atmospheric scale height (H: distance for $1/e$ decrease in density computed for hydrostatic equilibrium) in the lower stratosphere. At these distances, horizontal variations in temperature and composition are negligible. However, vertical variations can be substantial and, therefore, the measured spectral radiance by each detector is a convolution of the emerging radiance at each point in the FOV, weighted by the 1D average response cross section (see Eq. 1 of [10]):

$$\bar{I}(z_0) = \frac{\int R(z)I(z)\mathrm{d}z}{\int R(z)}, \tag{6}$$

where $I(z)$ is the radiance at altitude z, $R(z)$ is the detector response projected onto the limb, and $\bar{I}(z_0)$ is the weighted mean radiance resulting. Previously, [10] considered the effect of the finite FOV of CIRS detectors for all focal planes, approximating the FP1 spatial response by an idealized Gaussian profile, and the FP3 and FP4 detectors as 0.27×0.27 mrad uniform square fields. However, our measurements show that the actual FOVs for FP3 differ from idealized boxcar functions. In the next section we use synthetic spectral modeling combined with the laboratory data to show how the predicted radiances of the real MIR detectors can deviate measurably from the idealized uniform response.

A. Radiance Modeling

To test the effects of the field of view responses on the modeled radiances from Titan's limb, we follow the approach of [10]. First, we used the NEMESIS radiative transfer code [21] to create a fine 1 km grid of 501 synthetic spectra with tangent altitudes between 0 and 500 km. For these calculations we assumed the same equatorial reference atmosphere and spectroscopic data as [22] (see Fig. 10). We chose to test an equatorial retrieval because the gas VMR profiles are steepest at the equator (at the current time) and, hence, would be expected to show a larger systematic error due to a finite FOV than the flatter vertical profiles presently seen in the north.

Second, the fine grid of spectra was used to determine the modeled radiance for our standard Titan atmosphere by convolving the synthetic radiance at each wavenumber with three successively more realistic assumed FOV responses: A) infinitesimally small, B) boxcar functions, and C) the averaged detector responses in Table 4.

For an FOV that overlaps with M grid points in the range $l = m_1 - m_2$, the resulting modeled radiance $\bar{I}(\nu, z)$ at a given altitude z is given by Eq. 10 from [10]:

$$\bar{I}(\nu, z) = \sum_{l=m_1}^{m_2} w(z_l)I(\nu, z_l), \tag{7}$$

where $I(\nu, z_l)$ is the synthetic radiance for wavenumber ν calculated at gridpoint l with altitude z_l. The detector's normalized response at altitude z_l is $w(z_l)$. For the three test cases the normalized responses $w(z_l)$ are given by

Infinitesimal

$$w(z_l) = \delta(z), \tag{8}$$

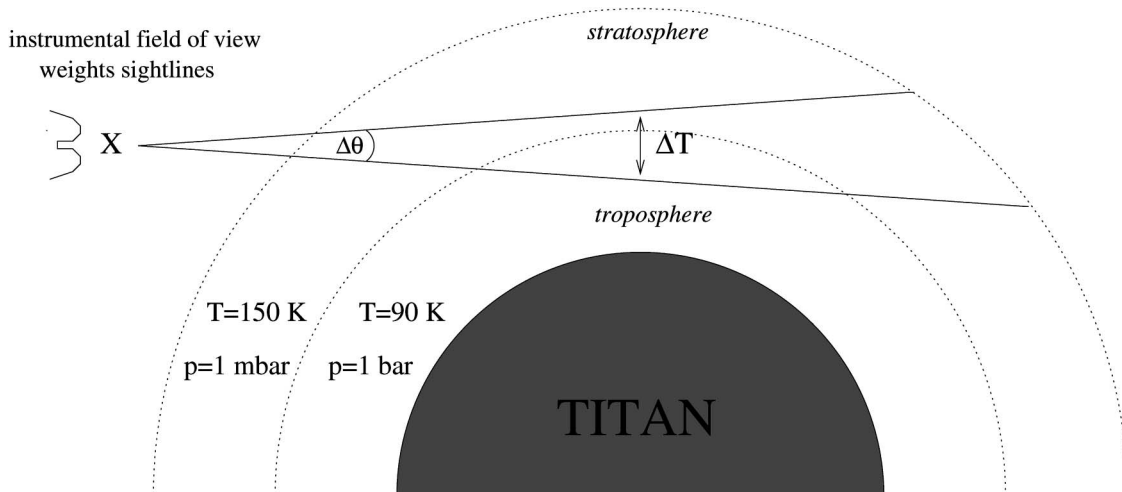where $\delta(\ )$ is the Dirac delta function.

Fig. 9. Simplified schematic diagram of CIRS limb-viewing geometry (FP3 detector depicted).
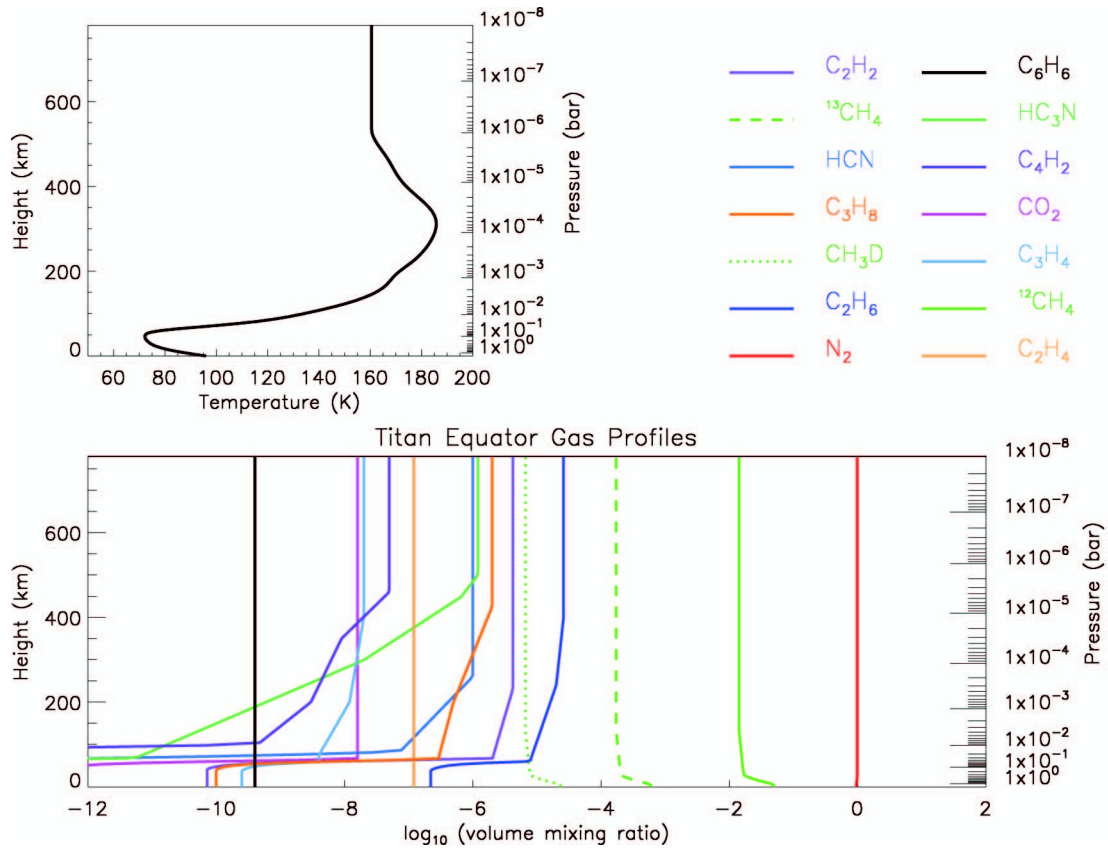
Fig. 10. *A priori* temperature (upper left) and gas VMR profiles (lower) used in synthetic spectra calculations. See text for details.

Boxcar

$$w(z_l) = \begin{cases} \frac{1}{2(M-1)} & \text{for: } l = m_1 \text{ and } m_2 \\ \frac{1}{M-1} & \text{for: } l = m_1 + 1, \ldots, m_2 - 1 \end{cases}, \quad (9)$$

as in [10].

Measured

$$w_n(z_l) = \frac{\bar{R}_n(z_l)}{\sum_{l=m_1}^{m_2} \bar{R}_n(z_l)}, \quad (10)$$

where $\overline{R}_n(z_l)$ is the Y-averaged response of the nth detector at altitude z_l, and the transformation from height coordinates to detector coordinates ($\Delta\theta$, interpolated from Table 4) is given by

$$z_l = z \pm d\Delta\theta, \quad (11)$$

where d is the spacecraft range to the tangent point, which is proportional to the FOV size, and the "±" accounts for the vertical orientation of the detector arrays: with $-Z$ of $+Z$ parallel to the normal to the limb (local vertical).

To determine the likely magnitude of radiance errors caused by assuming that the FOV is infinitesimally small or boxcar shaped, we take the difference between these approximations and that obtained using the true detector responses from Table 4.

The resulting radiance error is plotted in Fig. 11 as a function of altitude and wavenumber for a typical FP3/4 FOV size of 48 km. For smaller FOVs the errors will be proportionally less. As each detector has a different response, we have selected three representative detectors—one from FP4 and two from FP3.

For FP4, the uniform boxcar response assumed by [10] introduces an error of about $1 \text{nWcm}^{-2}\text{sr}^{-1}/\text{cm}^{-1}$, while the infinitesimal-ray approximation introduces at least $3 \text{nWcm}^{-2}\text{sr}^{-1}/\text{cm}^{-1}$, compared to an exact calculation with the real spatial response function. These errors may be compared to the typical noise equivalent spectral radiance (NESR) for a single scan in FP4 of around $4 \text{nWcm}^{-2}\text{sr}^{-1}/\text{cm}^{-1}$, indicating that only a few spectra need to be averaged together to reduce the NESR to levels comparable to the modeling error introduced by these assumptions.

For FP3, the pixel responses are not uniform and the double-lobed spatial weighting leads to an even greater effect than in FP4. Here the infinitesimal-ray approximation leads to a maximum error of $\sim 10 \text{nWcm}^{-2}\text{sr}^{-1}/\text{cm}^{-1}$. The boxcar approximation reduces errors to around $\sim 3 \text{nWcm}^{-2}\text{sr}^{-1}/\text{cm}^{-1}$, although there are substantial detector-to-detector variations. In comparison, the typical NESR for a single scan in FP3 is around $20 \text{nWcm}^{-2}\text{sr}^{-1}/\text{cm}^{-1}$,
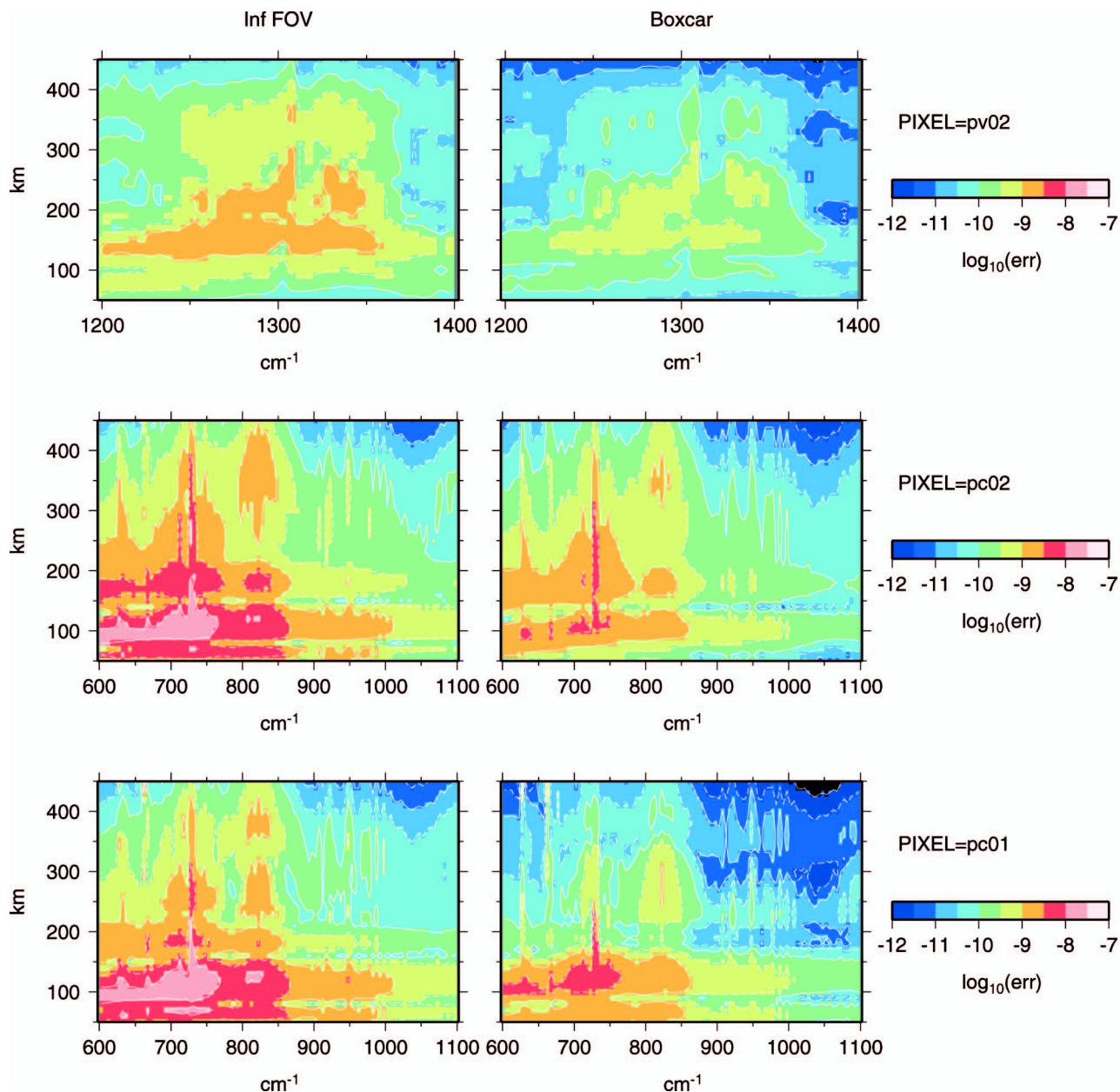
Fig. 11. Absolute radiance errors for infinitesimal FOVs (left) and boxcar shaped FOVs (right), assuming a 48 km projected FOV size. The plotted errors are the differences between synthetic radiances obtained by convolving a fine grid of synthetic spectra with the measured FOV responses in Table 4 and synthetic radiances calculated by assuming infinitesimal and boxcar-shaped FOVs. To make the plots more readable, the maximum error in $10 \, cm^{-1}$ wide bins is plotted.

or $2 \, nWcm^{-2}sr^{-1}/cm^{-1}$ for a relatively small limb average of 100 spectra, indicating that neither approximation may be sufficient for high accuracy fitting of such averages, at least in the cores of strong lines, such as the Q branch of C_2H_2 at $729 \, cm^{-1}$.

B. Vertical Profile Retrievals

Figure 12 illustrates the importance of incorporating the measured FOV shapes into atmospheric retrievals by considering a synthetic observation and test retrieval, which attempts to recover temperature and HCN profiles using infinitesimal, boxcar, and approximated real FOV responses. In this test a set of synthetic limb observations with tangent altitudes

from 100–500 km (spaced by 50 km) was created by convolving the measured FOV responses with the finely spaced 1 km grid of synthetics for a FOV FWHM of 48 km. The spectral resolution was $0.5 \, cm^{-1}$ as before. This test is representative of a CIRS MIR limb integration sequence, typically used for temperature and composition retrievals.

Note we assume here "perfect" knowledge of spacecraft pointing; or at least, that errors in actual spacecraft pointing deviate from commanded or reconstructed pointing by less than an atmospheric scale height. In general this is true: spacecraft pointing on reaction wheels is usually accurate to 1/4 to 1/2 of a MIR pixel, or better. (Thrusters, which
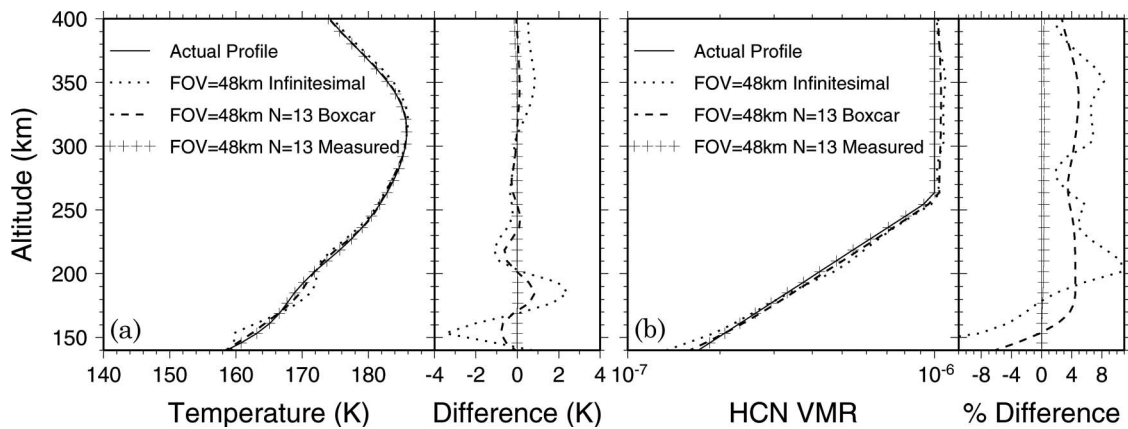
Fig. 12. Test retrievals from a $0.5\,\mathrm{cm}^{-1}$ resolution synthetic observation with a FOV size of $48\,\mathrm{km}$. (a) Temperature. Infinitesimal and boxcar approximations introduce spurious wiggles into the retrieved profiles. This could be significantly reduced by applying additional vertical smoothing to the retrieval. (b) HCN. Infinitesimal and boxcar approximations introduce 10% and 5% biases respectively into the retrieved profiles. The measured FOV response is required to remove this bias. For both tests, using a 13-point approximation to the measured FOV responses allows the starting profiles to be recovered accurately.

provide less accurate pointing, are only used for low flybys, and this does not apply to MIR limb sounding that occurs at greater distances.) On several occasions where it has deviated by more than one scale height (about one pixel) from the nominal pointing, the effect has been quite noticeable, as vertical temperature retrievals on FP4 that attempt to simultaneously fit multiple spectra at a range of altitudes cannot converge on a single temperature profile. Therefore, the offset can actually be included as a free but constrained parameter in the retrievals and accounted for.

We then attempted to retrieve temperature and HCN profiles from these noise-free spectra, as a pure test of the effect of the assumed FOV convolution. We used A) an infinitesimal FOV, B) a boxcar approximated FOV with $N = 13$, and C) the measured response approximated by $N = 13$ FOV averaging points. For temperature we used the 1265–$1345\,\mathrm{cm}^{-1}$ spectral region from FP4 and for HCN we used 705–$720\,\mathrm{cm}^{-1}$ from FP3. The retrieval method is explained in detail by [5,21]. Figure 12 shows that neglecting the shape of the measured FOVs introduces artifacts into the retrieved profiles, the infinitesimal approximation being the worst. Because of saturation of the contribution functions there is little information on atmospheric temperature and composition below about $140\,\mathrm{km}$, so lower altitudes are not shown.

For temperature, spurious wiggles are introduced for the infinitesimal and boxcar approximations. However, the mean error introduced oscillates about zero and would be effectively suppressed by imposing vertical smoothing during the retrieval. For HCN the effect of the detector FOVs is more serious and introduces a bias into the retrieved profile. The infinitesimal FOV causes an overestimation by about 10%, whereas the boxcar approximation reduces this to 5%. These discrepancies would not be removed by applying vertical smoothing to the retrieval. However,

using a $N = 13$ point approximation to the measured FOV responses effectively removes this bias.

C. Titan CO_2 Isotope Retrievals

In view of the results of the previous sections, which show that the real detector spatial responses can have a significant effect on retrieved parameters, we decided to repeat the retrieval of the carbon and oxygen isotopic ratios from CIRS limb spectra of CO_2 and its isotopologues in Titan's atmosphere, as published by [9]. In that study the least-realistic infinitesimal-ray approximation was used, although we expect that systematic biases in the retrieved gas abundances would be partly canceled when the abundances are ratioed to find the isotopic ratios, as the spectrum is mostly optically thin and the radiation therefore emanates from the same level (the limb tangent altitude) for all species.

For comparison to the infinitesimal-ray results, we repeated the retrievals of [9], changing only the treatment of the FOV. Three of the original four latitude cases were tested. In [9], spectra from multiple detectors and latitudes were averaged in an altitude range of 100–$150\,\mathrm{km}$. Therefore, for the boxcar approximation, we formed an effective spatial weighting function by coadding and averaging the boxcar functions for each individual spectrum, computed for the actual tangent altitude and projected FOV size on the limb as described in [11]. For the real response model, we also formed an effective spatial weighting function for the whole average as in the boxcar case, but in addition, using the actual FOV responses for the particular detector that recorded each spectrum. We did not include the real orientation of the FOV functions relative to the limb normal direction, but instead assumed the most common case where the $-Z$ direction of the detectors is parallel to the vertical. This will tend to form an upper limit on the actual effect, as a superposition of randomly oriented detector real FOVs will show less difference from the boxcar case.

Table 5. CO₂ Isotopic Abundance Retrievals[a]

Mean	$^{12}CO_2$(ppb)			$^{13}CO_2$(ppb)			$C^{16}O^{18}$(ppb)		
⟨Lat.⟩	A	B	C	A	B	C	A	B	C
−26	12.1 ± 0.5	11.6 ± 0.6	11.5 ± 0.6	11.4 ± 4.2	10.8 ± 4.0	10.0 ± 3.8	15.8 ± 9.1	14.2 ± 8.8	16.3 ± 9.2
9	17.8 ± 1.1	16.9 ± 1.1	17.0 ± 1.1	17.6 ± 7.2	17.8 ± 7.2	17.6 ± 7.2	21.7 ± 14.6	21.9 ± 15.4	22.3 ± 15.5
29	21.3 ± 1.3	21.1 ± 1.2	21.1 ± 1.2	20.7 ± 7.2	21.4 ± 7.5	21.5 ± 7.5	20.2 ± 13.7	23.9 ± 16.2	23.9 ± 16.2

[a]A, infinitesimal ray; B, boxcar approximation; and C, real FOV response.

The results for the gas retrievals are shown in Table 5. We find that the change in the VMRs in all cases is within the predicted $1 - \sigma$ random error bar of the original (infinitesimal-ray) retrieval, although in some cases at the edge of this range. We note that, in agreement with Subsection 3.B, the major $^{12}CO_2$ isotopologue is overestimated by about 5% in the infinitesimal-ray approximation compared to the real FOV calculation. The inferred molecular isotopic ratios (Table 6) are almost unchanged, as the systematic effects of the FOV modeling tend to be canceled in the ratio.

4. Discussion and Conclusions

We have considered the scientific importance of the spatial response functions of the Cassini CIRS MIR detectors. We first discussed the laboratory measurements made prior to launch, which gave us an accurate picture of the detector spatial responses, and then proceeded to show how these may influence scientific results if they are not properly included in the model.

We computed synthetic spectra for CIRS viewing of Titan's atmosphere by convolving single-ray spectra with idealized (boxcar) and actual detector spatial responses. For FP4, the error introduced by a single-ray approximation is as great as the single-scan NESR, and even the boxcar approximation has an error comparable to 1/4 of the single-scan NESR. Therefore, for even small averages of 16 spectra, the boxcar approximation would become the limit to spectral fitting. For FP3, the infinitesimal-ray error is 1/2 the single-scan NESR, while the boxcar error is 1/6 the NESR, so the situation is marginally better than for FP3.

In fact, it is a surprising conclusion of this paper that the boxcar approximation actually serves the U-shaped, asymmetric FP3 detectors better than those of FP4, which have a nominally much more boxcarlike spatial response. Why? The answer lies in the combination of the telescope PSF—which both smooths the FP3 responses and defocuses the sharp edges of the FP4 detector responses—and the much lower noise of the individual FP4 detectors. While the actual systematic error of the two idealized approximations is about 3× larger for FP3 than for FP4, the NESR on FP4 is about 1/4 that of FP3, and so the FOV approximation breaks down earlier. If the telescope function had not been included, the FP4 detectors would indeed have appeared very close to a boxcar response.

We have also investigated the effect of the real spatial responses on CIRS retrieval calculations, both synthetic and actual. We find that, while artifacts introduced into the retrieved temperature profile by an approximate FOV treatment may be suppressed by vertical smoothing, retrieved gas profiles, on the other hand, may be systematically overestimated. Our actual retrieval tests for CO_2 seem to bear this out, at least for the major isotopologue, where the VMR is indeed overestimated by 5% in the single-ray retrieval. Fortunately, the isotopic ratios were unaffected by the FOV modeling, due to approximate cancellation between gas species.

We therefore conclude that, for small averages of ∼20 spectra, which occurs in practice for limb sounding of a single profile on a single flyby with no coadding across detectors, the boxcar approximation may be sufficiently accurate provided that appropriate vertical smoothing is used for FP4 temperature retrievals. However, for other investigations, such as measurements of very weak trace species, where several hundreds of spectra are coadded, the real FOV responses must be used in modeling if the S/N is not to be limited by systematic model error. Indeed, now that the measured detector spatial responses have been studied in detail and provided in this work, it is a small effort to include them in all CIRS limb modeling and thereby eliminate entirely this source of systematic error.

Table 6. Isotopic Ratios from CO₂ Retrievals[a]

Lat.	Mean		$CO_2/^{13}CO_2$			$CO_2/C^{16}O^{18}O$		
Range	⟨Lat.⟩	N_{spec}	A	B	C	A	B	C
35 °S–15 °S	−26	183	96 ± 36	96 ± 36	95 ± 36	185 ± 107	197 ± 36123	177 ± 101
00 °N–20 °N	9	162	80 ± 33	78 ± 32	79 ± 33	190 ± 128	193 ± 137	191 ± 150
25 °N–35 °N	29	224	78 ± 27	81 ± 29	81 ± 28	224 ± 153	221 ± 150	221 ± 150
Mean			83 ± 18	84 ± 18	84 ± 18	195 ± 72	202 ± 78	190 ± 71

[a]A, infinitesimal ray; B, boxcar approximation; and C, real FOV response.

References

1. F. M. Flasar, V. G. Kunde, M. M. Abbas, R. K. Achterberg, P. Ade, A. Barucci, B. Bézard, G. L. Bjoraker, J. C. Brasunas, S. Calcutt, R. Carlson, C. J. Césarsky, B. J. Conrath, A. Coradini, R. Courtin, A. Coustenis, S. Edberg, S. Edgington, C. Ferrari, T. Fouchet, D. Gautier, P. J. Gierasch, K. Grossman, P. Irwin, D. E. Jennings, E. Lellouch, A. A. Mamoutkine, A. Marten, J. P. Meyer, C. A. Nixon, G. S. Orton, T. C. Owen, J. C. Pearl, R. Prangé, F. Raulin, P. L. Read, P. N. Romani, R. E. Samuelson, M. E. Segura, M. R. Showalter, A. A. Simon-Miller, M. D. Smith, J. R. Spencer, L. J. Spilker, and F. W. Taylor, "Exploring the Saturn system in the thermal infrared: the composite infrared spectrometer," Space Sci. Rev. **115**, 169–297 (2004).

2. V. G. Kunde, P. A. R. Ade, R. D. Barney, D. Bergman, J.-F. Bonnal, R. Borelli, D. Boyd, J. C. Brasunas, G. V. Brown, S. B. Calcutt, F. Carroll, R. Courtin, J. B. Cretolle, J. A. Crooke, M. A. Davis, S. Edberg, R. K. Fettig, M. Flasar, D. A. Glenar, S. Graham, J. G. Hagopian, C. F. Hakun, P. A. Hayes, L. Herath, L. Spilker, D. E. Jennings, G. Karpati, C. Kellebenz, B. Lakew, J. Lindsay, J. Lohr, J. J. Lyons III, R. J. Martineau, A. J. Martino, M. Matsumura, J. McCloskey, T. Melak, G. Michel, A. Morrell, C. Mosier, L. G. Pack, M. Plants, D. Robinson, L. Rodriguez, P. Romani, B. Schaefer, S. M. Schmidt, C. Trujillo, T. Vellacott, K. Wagner, and D. Yun, "Cassini infrared Fourier spectroscopic investigation," Proc. SPIE **2803**, 162–177 (1996).

3. R. Hanel, B. Conrath, V. G. Kunde, P. Lowman, W. Maguire, J. Pearl, J. Pirraglia, D. Gautier, P. Gierasch, and S. Kumar, "The Voyager infrared spectroscopy and radiometry investigation," Space Sci. Rev. **21**, 129–157 (1977).

4. A. Coustenis, D. E. Jennings, A. Jolly, Y. Bénilan, C. A. Nixon, S. Vinatier, D. Gautier, G. L. Bjoraker, P. N. Romani, R. C. Carlson, and F. M. Flasar, "Detection of C_2HD and the D/H ratio on Titan," Icarus **197**, 539–548 (2008).

5. N. A. Teanby, P. G. J. Irwin, R. de Kok, S. Vinatier, B. Bézard, C. A. Nixon, F. M. Flasar, S. B. Calcutt, N. E. Bowles, L. Fletcher, C. Howett, and F. W. Taylor, "Vertical profiles of HCN, HC_3N and C_2H_2 in Titan's atmosphere derived from Cassini/CIRS data," Icarus **186**, 364–384 (2007).

6. S. Vinatier, B. Bézard, and C. A. Nixon, "The Titan $^{14}N/^{15}N$ and $^{12}C/^{13}C$ isotopic ratios in HCN from Cassini/CIRS," Icarus **191**, 712–721 (2007).

7. S. Vinatier, B. Bézard, T. Fouchet, N. A. Teanby, R. de Kok, P. G. J. Irwin, B. J. Conrath, C. A. Nixon, P. N. Romani, F. M. Flasar, and A. Coustenis, "Vertical abundance profiles of hydrocarbons in Titan's atmosphere at 15 °S and 15 °N retrieved from Cassini/CIRS spectra," Icarus **188**, 120–138 (2007).

8. D. E. Jennings, C. A. Nixon, A. Jolly, B. Bézard, A. Coustenis, S. Vinatier, P. G. J. Irwin, N. A. Teanby, P. N. Romani, R. K. Achterberg, and F. M. Flasar, "Isotopic ratios in Titan's atmosphere from Cassini CIRS limb sounding: HC_3N in the north," Astrophys. J. Lett. **681**, L109–L111 (2008).

9. C. A. Nixon, D. E. Jennings, B. Bézard, N. A. Teanby, R. K. Achterberg, A. Coustenis, S. Vinatier, P. G.J. Irwin, P. N. Romani, T. Hewagama, and F. M. Flasar, "Isotopic ratios in Titan's atmosphere from Cassini CIRS limb sounding: CO_2 in the equator and south," Astrophys. J. Lett. **681**, L101–L103 (2008).

10. N. A. Teanby and P. G. J. Irwin. "Quantifying the effect of finite field-of-view size on radiative transfer calculations of Titan's limb spectra measured by Cassini-CIRS," Astrophys. Space Sci. **310**, 293–305 (2007).

11. C. A. Nixon, D. E. Jennings, J.-M. Flaud, B. Bézard, N. A. Teanby, P. G. J. Irwin, T. M. Ansty, A. Coustenis, and F. M. Flasar, "Titan's prolific propane: the Cassini CIRS perspective," Planet. Space Sci. (submitted).

12. N. A. Teanby, P. G. J. Irwin, R. de Kok, A. Jolly, B. Bézard, C. A. Nixon, and S. B. Calcutt, "Titan's stratospheric C_2N_2, C_3H_4 and C_4H_2 abundances from Cassini/CIRS far-infared spectra.," Icarus (submitted).

13. N. A. Teanby, P. G. J. Irwin, R. de Kok, C. A. Nixon, A. Coustenis, E. Royer, S. B. Calcutt, N. E. Bowles, L. Fletcher, C. Howett, and F. W. Taylor, "Global and temporal variations in hydrocarbons and nitriles in Titan's stratosphere for northern winter observed by Cassini/CIRS," Icarus **193**, 595–611 (2008).

14. N. A. Teanby, R. de Kok, P. G. J. Irwin, S. Osprey, S. Vinatier, P. J. Gierasch, P. L. Read, F. M. Flasar, B. J. Conrath, R. K. Achterberg, B. Bézard, C. A. Nixon, and S. B. Calcutt, "Titan's polar vortex structure revealed by chemical tracers," J. Geophys. Res. **113**, E12003 (2008).

15. C. A. Nixon, "Remote sounding of the atmosphere of Titan," PhD dissertation (University of Oxford, 1998).

16. D. H. Martin and E. Puplett, "Polarized interferometric spectroscopy for the millimeter and submillimeter spectrum," Infrared Phys. **10**, 105–109 (1970).

17. R. A. Hanel, B. J. Conrath, D. E. Jennings, and R. E. Samuelson, *Exploration of the Solar System by Infrared Remote Sensing*, 2nd ed. (Cambridge U. Press, 2003).

18. D. Glenar, "Recreating the CIRS FP3 I&T Y-RASTER data," unpublished memo (January 1998).

19. D. Glenar, R. Carlson, and V. Kunde. "Science performance review: CIRS pre-ship review," Technical report (NASA, Goddard Space Flight Center, 1997).

20. M. D. Smith, "CIRS boresight test of April 28/29 2001," Technical report (NASA, Goddard Space Flight Center, May 2001).

21. P. G. J. Irwin, N. A. Teanby, R. de Kok, L. N. Fletcher, C. J. A. Howett, C. Tsang, C. Wilson, S. B. Calcutt, C. A. Nixon, and P. Parrish, "The NEMESIS planetary atmosphere radiative transfer and retrieval tool," J. Quant. Spectrosc. Radiat. Transfer **109**, 1136–1150 (2008).

22. N. A. Teanby, P. G. J. Irwin, R. de Kok, C. A. Nixon, A. Coustenis, B. Bézard, S. B. Calcutt, N. E. Bowles, F. M. Flasar, L. Fletcher, C. Howett, and F. W. Taylor, "Latitudinal variations of HCN, HC_3N and C_2N_2 in Titan's stratosphere derived from Cassini CIRS data," Icarus **181**, 243–255 (2006).